

Maximum Energy of Particles Accelerated in GRB Afterglow Shocks

ZHAO-FENG WU,¹ SOFÍA GUEVARA-MONTOYA,² PAZ BENIAMINI,^{3,4,5} DIMITRIOS GIANNIOS,¹ DANIEL GROŠELJ,⁶ AND LORENZO SIRONI^{7,8}

¹Department of Physics and Astronomy, Purdue University, 525 Northwestern Avenue, West Lafayette, IN 47907, USA

²Departamento de Física, Universidad Nacional de Colombia, Bogotá 111321, Colombia

³Department of Natural Sciences, The Open University of Israel, P.O. Box 808, Ra'anana 4353701, Israel

⁴Astrophysics Research Center of the Open University (ARCO), The Open University of Israel, P.O. Box 808, Ra'anana 4353701, Israel

⁵Department of Physics, The George Washington University, 725 21st Street NW, Washington, DC 20052, USA

⁶Centre for mathematical Plasma Astrophysics, Department of Mathematics, KU Leuven, B-3001 Leuven, Belgium

⁷Department of Astronomy and Columbia Astrophysics Laboratory, Columbia University, New York, NY 10027, USA

⁸Center for Computational Astrophysics, Flatiron Institute, 162 5th Avenue, New York, NY 10010, USA

ABSTRACT

Particle acceleration in relativistic collisionless shocks remains an open problem in high-energy astrophysics. Particle-in-cell (PIC) simulations predict that electron acceleration in weakly magnetized shocks proceeds via small-angle scattering, leading to a maximum electron energy significantly below the Bohm limit. This upper bound manifests observationally as a characteristic synchrotron cutoff, providing a direct probe of the underlying acceleration physics. Gamma-ray burst (GRB) afterglows offer an exceptional laboratory for testing these predictions. Here, we model the spectral evolution of GRB afterglows during the relativistic deceleration phase, incorporating PIC-motivated acceleration prescriptions and self-consistently computing synchrotron and synchrotron self-Compton emission. We find that low-energy bursts in low-density environments, typical of short GRBs, exhibit a pronounced synchrotron cutoff in the GeV band within minutes to hours after the trigger. Applying our framework to GRB 190114C and GRB 130427A, we find that current observations are insufficient to discriminate between PIC-motivated acceleration and the Bohm limit, primarily due to large uncertainties in the Fermi-LAT band. Nevertheless, future MeV–TeV afterglow observations can break model degeneracies and place substantially tighter constraints on particle acceleration in relativistic shocks.

Keywords: High energy astrophysics (739) — Shocks (2086) — Non-thermal radiation sources (1119) — Plasma astrophysics (1261) — Gamma-ray bursts (629) — Relativistic jets (1390)

1. INTRODUCTION

Relativistic collisionless shocks are among the most efficient particle accelerators in the Universe. Their signatures are observed across a wide range of astrophysical environments, yet the physical mechanisms governing particle acceleration in these systems remain poorly understood (R. Barniol Duran & P. Kumar 2011; E. Sagi & E. Nakar 2012; L. Sironi et al. 2015). One of the leading candidates is the diffusive shock acceleration process, in which particles gain energy through repeated crossings of the shock front mediated by magnetic turbulence (e.g., E. Fermi 1949; L. Sironi & A. Spitkovsky 2011; A. R. Bell 1978; R. D. Blandford & J. P. Ostriker

1978; A. Achterberg et al. 2001). In the most optimistic scenario, the scattering mean free path approaches the Larmor radius of the accelerated particle, corresponding to the so-called Bohm limit (O. C. de Jager & A. K. Harding 1992), which represents the theoretical upper bound on acceleration rate.

The non-linear processes taking place at the shock front can be modeled from first principles using particle-in-cell (PIC) simulations, which have substantially advanced our understanding of particle acceleration at relativistic shocks (e.g., A. Spitkovsky 2008a,b; S. F. Martins et al. 2009; L. Sironi et al. 2015). In weakly magnetized environments, simulations show that particle acceleration proceeds via small-angle scattering, leading to a slower increase of the maximum electron Lorentz factor, $\gamma_{\max} \propto t^{1/2}$, rather than the linear growth expected

in the Bohm limit (U. Keshet et al. 2009; J. G. Kirk & B. Reville 2010; I. Plotnikov et al. 2013; L. Sironi et al. 2013; D. Grošelj et al. 2024).

Gamma-ray bursts (GRBs) provide an exceptional laboratory for testing particle acceleration predictions. In the standard afterglow framework, the interaction between the relativistic ejecta and the circumburst medium results into a forward shock that accelerates electrons, producing broadband emission via synchrotron and synchrotron self-Compton (SSC) radiation (e.g., R. Sari et al. 1998; R. Sari & A. A. Esin 2001; D. Miceli & L. Nava 2022). When radiative losses are taken into account, particle acceleration is limited to a maximum Lorentz factor, leading to a characteristic cutoff in the synchrotron spectrum (L. Sironi et al. 2013). For typical GRB parameters, this cutoff is expected to appear in the GeV band during the early afterglow phase. Detecting such a feature would therefore provide a direct and robust probe of the microphysics governing particle acceleration in relativistic shocks.

Observationally, however, identifying the synchrotron cutoff remains challenging. Although Fermi-LAT has enabled systematic detections of long-lived GeV emission from GRB afterglows, a clear synchrotron cutoff has not been observed yet (M. Ajello et al. 2019), likely due to dominance of a rising SSC component. In such a case, the observed spectrum does not necessarily exhibit a sharp cutoff, but instead shows a spectral hardening around GeV (A. Panaitescu 2017; X.-B. He et al. 2022). Instrumental sensitivity and photon statistics limitations in the GeV band further hinder the identification of both cutoff and spectral hardening features (M. Ajello et al. 2019).

Recent detections of very-high-energy (VHE; $\gtrsim 300$ GeV) emission from GRB afterglows by ground-based Cherenkov telescopes, such as MAGIC (J. Aleksić et al. 2016a,b), directly sample the SSC component and help break degeneracies in spectral modeling (V. A. Acciari et al. 2019a), enabling more robust observational probes of the particle acceleration timescales. By combining GeV and TeV observations with X-ray data, one can place significantly tighter constraints on the maximum synchrotron photon energy and, consequently, on the underlying particle acceleration physics.

In this paper, we test PIC-motivated particle acceleration models for weakly magnetized collisionless shocks in the context of GRB afterglow observations. We implement acceleration prescriptions motivated by the PIC simulations and by the Bohm diffusion limit within a self-consistent numerical framework for modeling GRB afterglow spectra. We show that low-energy bursts in low-density environments are most likely to yield a de-

tectable synchrotron cutoff. Applying our model to GRB 190114C and GRB 130427A, we assess current observational constraints and discuss prospects for future detections.

2. METHODOLOGY

We first discuss particle acceleration models and their associated spectral cutoffs for relativistic shocks in general, and then incorporate them in the context of GRB afterglows. Throughout this work, primed quantities denote values measured in the post-shock fluid comoving frame, lowercase unprimed quantities refer to the central engine frame, and uppercase quantities correspond to the observer frame, unless stated otherwise. Gaussian-cgs units are used throughout.

2.1. Particle Acceleration Prescription

Weakly magnetized relativistic shocks are expected to accelerate electrons into a nonthermal power-law distribution (e.g., A. Achterberg et al. 2001) of the form

$$n'(\gamma) \propto \gamma^{-p} \quad (1)$$

valid over the range $\gamma_{\min} \leq \gamma \leq \gamma_{\max}$, where p is the power-law index and γ is the electron Lorentz factor measured in the frame comoving with the shocked fluid. Hereafter, all electron Lorentz factors γ are defined in the comoving frame. Assuming a pure power-law electron distribution, the minimum Lorentz factor is determined by the shock jump conditions (R. Sari et al. 1996) and can be written as

$$\gamma_{\min} \simeq \varepsilon_e \frac{p-2}{p-1} \frac{m_p}{m_e} \Gamma, \quad (2)$$

where ε_e is the fraction of post-shock internal energy carried by electrons, m_e and m_p are the electron and proton masses, respectively, and Γ is the bulk Lorentz factor of the shocked fluid. The expression is valid in the limit $\gamma_{\min} \ll \gamma_{\max}$ with typical spectral indices $p \simeq 2.4$.⁹

PIC simulations performed in the past couple of decades indicate that electrons accelerated at relativistic shocks form a nonthermal power-law distribution with index $p \simeq 2.4$ and an energy fraction $\varepsilon_e \sim 0.1$ for weakly magnetized shocks (e.g., L. Sironi et al. 2013). In addition, studies of GRB afterglows suggest that $\varepsilon_e \sim 0.1 - 0.15$ with little scatter (L. Nava et al. 2014; P. Beniamini & A. J. van der Horst 2017). More recent PIC studies suggest the possible emergence of an

⁹ For $p \simeq 2$, the dependence of γ_{\min} on the high-energy cutoff becomes non-negligible. In our calculations, we use the full expression that accounts for both γ_{\max} and p , although the difference is negligible for the parameter values considered here.

additional structure in the particle spectrum, including a suprathermal component, toward the end of the simulation (D. Grošelj et al. 2024). A detailed exploration of these effects is beyond the scope of this work. Throughout this study, we adopt $\varepsilon_e = 0.1$ and assume a power-law index of $p \simeq 2.4$.

The maximum electron Lorentz factor γ_{\max} is determined by balancing the acceleration rate against synchrotron cooling losses, as SSC losses are strongly suppressed in the deep Klein–Nishina (KN) regime. We consider two representative particle acceleration prescriptions, which differ in their acceleration rates and therefore predict different maximum attainable energies.

The first acceleration model is motivated by PIC simulations (e.g., L. Sironi et al. 2013; I. Plotnikov et al. 2018; D. Grošelj et al. 2024), which indicate small-angle scattering at the shock front. In this framework, the maximum electron Lorentz factor grows with time as $\gamma_{\max, \text{PIC}}(t') \propto (\omega_p t')^{1/2}$, and the acceleration rate can be written as

$$\gamma_{\max, \text{PIC}} \frac{d\gamma_{\max, \text{PIC}}}{dt'} = 0.25 \left(\frac{m_p}{m_e} \right)^2 \omega_p \Gamma^2 \varepsilon_B \left(\frac{\lambda' \omega_p}{c} \right), \quad (3)$$

where the $(m_p/m_e)^2$ factor reflects the assumption, motivated by PIC simulations, that the maximum electron energy can keep up with the maximum ion energy if cooling is neglected. Here λ' is the transverse coherence length of the magnetic field, ω_p is the frame-independent proton plasma frequency of the ambient medium (A. Achterberg & J. Wiersma 2007),

$$\omega_p \equiv \sqrt{4\pi e^2 n/m_p} \simeq 1.3 \times 10^3 n_0^{1/2} \text{ Hz}, \quad (4)$$

where $n = n_0 \text{ cm}^{-3}$, and ε_B is the magnetic energy fraction¹⁰ defined as

$$\varepsilon_B \equiv \frac{B'^2}{8\pi\Gamma^2 n m_p c^2}. \quad (5)$$

Recent simulations (D. Grošelj et al. 2024) suggest that $\varepsilon_B(\lambda' \omega_p/c) \simeq 0.4$, although this combination may be increasing for longer simulations. When synchrotron cooling is included, the evolution of the maximum electron Lorentz factor is governed by

$$\frac{d\gamma_{\max, \text{PIC}}}{dt'} \simeq \left(\frac{m_p}{m_e} \right)^2 \frac{0.1 \omega_p \Gamma^2}{\gamma_{\max, \text{PIC}}} - \frac{\sigma_T \gamma_{\max, \text{PIC}}^2}{6\pi} \frac{B'^2}{m_e c}. \quad (6)$$

All quantities are evaluated in the comoving frame of the shocked fluid, with t' denoting comoving time and

B' the comoving magnetic field strength. Balancing acceleration and synchrotron cooling yields an equilibrium Lorentz factor and represents the maximum attainable electron energy,

$$\gamma_{\max, \text{PIC}} = \left(\frac{0.6\pi m_p^2 \omega_p \Gamma^2 c}{\sigma_T m_e B'^2} \right)^{1/3} = 1.3 \times 10^7 n_0^{-1/6} \varepsilon_{B, -2.5}^{-1/3}, \quad (7)$$

where $\varepsilon_B = 10^{-2.5} \varepsilon_{B, -2.5}$.

For relativistic outflows with $\Gamma \gtrsim 100$, γ_{\max} is typically reached within seconds in the observer frame. An analytic estimate for the acceleration timescale is

$$T_{\text{PIC}} \simeq \frac{\gamma_{\max, \text{PIC}}}{\Gamma} \left(\frac{0.1 m_p^2 \omega_p \Gamma^2}{m_e^2 \gamma_{\max, \text{PIC}}} \right)^{-1} = 0.4 \Gamma_2^{-3} n_0^{-5/6} \varepsilon_{B, -2.5}^{-2/3} \text{ s}, \quad (8)$$

where $\Gamma = 100\Gamma_2$. This upper cutoff in the electron distribution should manifest as an exponential cutoff in the observed synchrotron spectrum. We can compute the corresponding characteristic synchrotron frequency for γ_{\max} , which serves as the beginning of the cutoff (R. Sari et al. 1998),

$$h\nu_{\max, \text{PIC}} = \frac{h\Gamma e B' \gamma_{\max, \text{PIC}}^2}{2\pi m_e c} \simeq 0.2 \Gamma_2^2 n_0^{1/6} \varepsilon_{B, -2.5}^{-1/6} \text{ GeV}. \quad (9)$$

The expressions for $\gamma_{\max, \text{PIC}}$ and $h\nu_{\max, \text{PIC}}$ derived above depend on the magnetic field properties in the vicinity of the shock, in particular the magnetic energy fraction ε_B and the coherence scale λ' , which regulate particle diffusion and cooling losses. However, extrapolating these parameters from the simulation scales to the astrophysical scales remains uncertain. Moreover, some studies indicate that the magnetic field may decay downstream of the shock front (P. Chang et al. 2008; P. Kumar et al. 2012; M. Lemoine 2013, 2015a,b), implying that the ε_B averaged over the full emission region can be lower than its value immediately behind the shock. The highest-energy particles predominantly cool close to the shock, while lower-energy particles are more sensitive to the averaged ε_B over the whole emission region.

While the evolution of magnetic field properties could in principle be treated with a multi-zone model, both $\gamma_{\max, \text{PIC}}$ and $h\nu_{\max, \text{PIC}}$ depend only weakly on ε_B . Therefore, the high-energy cutoff properties remain largely insensitive to moderate variations in ε_B , provided that the combination $\varepsilon_B(\lambda' \omega_p/c) \simeq 0.4$ is preserved. This motivates the use of an effective one-zone description. Consequently, and to remain consistent with PIC simulation results, we allow ε_B to vary only modestly towards lower values relative to our reference value of $\langle \varepsilon_B \rangle \simeq 3.5 \times 10^{-3}$. Specifically, we explore the range $10^{-4} \lesssim \varepsilon_B \lesssim 5 \times 10^{-3}$ while keeping

¹⁰ We adopt the same definition of ε_B as in L. Sironi et al. (2013) and D. Grošelj et al. (2024).

$\varepsilon_B(\lambda' \omega_p/c) \simeq 0.4$ fixed, following a prescription similar to that adopted by L. Sironi et al. (2013). Such values are also consistent with inferences from GRB afterglow modeling (R. Santana et al. 2014; P. Beniamini et al. 2015). A full treatment using a multi-zone model is left for future work.

For Bohm diffusion (O. C. de Jager & A. K. Harding 1992), electrons gain energy by a factor of order unity per gyration, corresponding to large-angle scattering that is significantly faster than small-angle scattering predicted by PIC simulations. Following the same balance between acceleration and synchrotron cooling, the maximum Lorentz factor becomes

$$\gamma_{\max, \text{Bohm}} = \sqrt{\frac{6\pi e}{\sigma_T B'}} = 1.1 \times 10^8 \varepsilon_{B,-2.5}^{-1/4} \Gamma_2^{-1/2} n_0^{-1/4}. \quad (10)$$

In this case, $\gamma_{\max, \text{Bohm}}$ increases as the jet decelerates. The corresponding acceleration timescale and characteristic synchrotron frequency are

$$T_{\text{Bohm}} \simeq \frac{\gamma_{\max, \text{Bohm}}}{\Gamma} \left(\frac{m_e c}{e B'} \right) = 5 \Gamma_2^{-5/2} n_0^{-1/4} \varepsilon_{B,-2.5}^{-3/4} \text{ s}, \quad (11)$$

and

$$h\nu_{\max, \text{Bohm}} = \frac{h \Gamma e B' \gamma_{\max, \text{Bohm}}^2}{2\pi m_e c} = 17.4 \Gamma_2 \text{ GeV}. \quad (12)$$

We note that $h\nu_{\max, \text{Bohm}}$ is independent of n and ε_B and remains fixed in the comoving frame of the shocked fluid. Bohm diffusion is considered to give a theoretical upper bound for γ_{\max} and $h\nu_{\max}$, which is, however, not supported by present PIC simulations of relativistic weakly magnetized shocks. The ratio of the cutoff energies predicted by the two prescriptions is

$$\frac{h\nu_{\max, \text{PIC}}}{h\nu_{\max, \text{Bohm}}} \simeq 0.01 \Gamma_2 n_0^{1/6} \varepsilon_{B,-2.5}^{-1/6} \quad (13)$$

indicating a difference of roughly two orders of magnitude that decreases for faster outflows, that depends linearly on the bulk Lorentz factor and very weakly on other physical parameters.

2.2. Dynamics of GRB Shocks

Powerful relativistic shocks in GRBs are generated as the ejecta from the central engine interact with the ambient medium. Here we introduce the dynamics of GRB shocks relevant for modeling GRB afterglow spectra.

The relativistic ejecta initially propagate into the ambient medium with a constant Lorentz factor Γ_0 . After sweeping up an external mass of order M_0/Γ_0 , where M_0 is the initial ejecta mass, the shell begins to decelerate and approaches the self-similar solution described

by R. D. Blandford & C. F. McKee (1976). In this work, we assume that the shock has already entered the self-similar deceleration phase and neglect the contribution of the reverse shock. Although the reverse shock can affect the dynamics prior to the deceleration radius r_{dec} (R. Sari & T. Piran 1995), its influence is confined to the very early evolution and is therefore expected to have a limited impact on the considerations here.

We focus on jets that propagate into a low-density ISM-like medium, which is the most relevant case for this work (see Section 3), rather than into the dense winds expected from massive progenitors (e.g., Wolf-Rayet stars; see P. A. Crowther 2007 for a review). Under the assumption of adiabatic expansion into a constant-density ISM, the bulk Lorentz factor of the shocked fluid¹¹ during the relativistic deceleration phase follows the self-similar solution of R. D. Blandford & C. F. McKee (1976),

$$\Gamma(r) = \left(\frac{17E_{\text{iso}}}{16\pi n m_p c^2} \right)^{\frac{1}{2}} r^{-\frac{3}{2}}, \quad (14)$$

valid at radii larger than the deceleration radius

$$r_{\text{dec}} \equiv \left(\frac{17E_{\text{iso}}}{16\pi \Gamma_0^2 n m_p c^2} \right)^{\frac{1}{3}} \quad (15)$$

where E_{iso} is the isotropic-equivalent explosion kinetic energy, Γ_0 is the initial Lorentz factor of the outflow, and n is the ambient number density measured in the rest frame of the ISM. Writing $E_{\text{iso}} = 10^{54} E_{\text{iso}, 54}$ erg and $\Gamma_0 = 10^{2.5} \Gamma_{0,2.5}$, the deceleration radius becomes

$$r_{\text{dec}} \simeq 1.3 \times 10^{17} \Gamma_{0,2.5}^{-2/3} E_{\text{iso}, 54}^{1/3} n_0^{-1/3} \text{ cm}. \quad (16)$$

During the relativistic deceleration phase, the observed emission is shaped by relativistic effects encapsulated in the Doppler factor,

$$\mathcal{D} = \frac{1}{\Gamma(1 - \beta \cos \theta)}, \quad (17)$$

where β is the dimensionless speed of the emitting region and θ is the angle between the emitting region and the observer's line of sight. For on-axis emission, $\mathcal{D} \simeq 2\Gamma$, while emission from regions with $\theta \gtrsim 1/\Gamma$ is strongly suppressed by relativistic beaming. After averaging over the visible emitting region of angular size $\sim 1/\Gamma$, the effective Doppler factor is well approximated by $\mathcal{D} \simeq \Gamma$ (T.

¹¹ This refers to the Lorentz factor of the shocked material immediately behind the shock front; the shock Lorentz factor itself is $\Gamma_{\text{sh}} = \sqrt{2} \Gamma$.

(Piran & E. Nakar 2010). The observed and comoving timescales are then related by

$$dT = \frac{(1+z)dt}{\Gamma^2} = \frac{(1+z)dt'}{\Gamma}. \quad (18)$$

where T , t and t' denote the observer, lab-frame and comoving times, respectively.

We now incorporate the shock dynamics into the spectral cutoffs discussed in Section 2.1. For the PIC-motivated acceleration prescription, the maximum Lorentz factor $\gamma_{\max, \text{PIC}}$ is independent of the bulk Lorentz factor Γ and therefore remains constant during the deceleration phase. In contrast, the maximum Lorentz factor under the Bohm diffusion limit evolves as

$$\gamma_{\max, \text{Bohm}} = 8 \times 10^7 \varepsilon_{B,-2.5}^{-1/4} E_{\text{iso},54}^{-1/16} n_0^{-3/16} T_{\text{obs},2}^{3/16}, \quad (19)$$

where $T_{\text{obs},2}$ is the observer time in units of 100 s. The corresponding characteristic synchrotron cutoff frequency for the PIC model is

$$h\nu_{\max, \text{PIC}} \simeq 0.8 \varepsilon_{B,-2.5}^{-1/6} E_{0,54}^{1/4} n_0^{-1/12} T_{\text{obs},2}^{-3/4} (1+z)^{-1/4} \text{ GeV}, \quad (20)$$

while for the Bohm limit it becomes

$$h\nu_{\max, \text{Bohm}} \simeq 35 E_{0,54}^{1/8} n_0^{-1/8} T_{\text{obs},2}^{-3/8} (1+z)^{-5/8} \text{ GeV}. \quad (21)$$

The ratio of the two cutoff frequencies is then

$$\frac{h\nu_{\max, \text{PIC}}}{h\nu_{\max, \text{Bohm}}} \simeq 0.02 \varepsilon_{B,-2.5}^{-1/6} E_{0,54}^{1/8} n_0^{1/24} T_{\text{obs},2}^{-3/8} (1+z)^{3/8}, \quad (22)$$

which depends weakly on the burst parameters and shows a modest evolution with observer time.

The radial extent of the radiative zone requires more careful treatment. High-energy particles and pressure are concentrated within a thin shell immediately behind the shock front, whereas material advected farther downstream undergoes significant adiabatic expansion and experiences a decayed magnetic field, contributing negligibly to the high-energy emission. We therefore define the emitting region up to the similarity variable $\chi = 2$ in the Blandford–McKee solution (R. D. Blandford & C. F. McKee 1976). The corresponding shell thickness in the comoving frame of the shocked fluid is

$$\Delta'(r) = \frac{r}{16\Gamma}, \quad (23)$$

appropriate for a constant density medium.

Here, we adopt a single-zone approximation and assume that the bulk Lorentz factor of the emitting plasma is equal to that immediately behind the shock. In the comoving frame of the fluid just behind the shock, material at the downstream border of the emitting shell

($\chi = 2$) recedes at a speed of $c/3$. The particle escape timescale from the radiative region can therefore be expressed as

$$t'_{\text{esc}} = \frac{\Delta'(r)}{c/3} = \frac{3r}{16\Gamma c}, \quad (24)$$

and the comoving volume of the emitting region is then given by

$$V' = \pi \left(\frac{r}{\Gamma} \right)^2 \Delta'(r) = \frac{\pi r^3}{16\Gamma^3}. \quad (25)$$

Here we do not account for the finite opening angle of the jet and instead approximate the outflow as spherical. This approximation is justified because the luminosity per unit solid angle is effectively identical to that of a spherical explosion as long as the relativistic beaming angle is smaller than the jet opening angle. The former increases over time, and the two eventually become equal at the ‘jet break time’ (e.g., J. E. Rhoads 1997; R. Sari et al. 1999). Such a break occurs long after the early sub-GeV emission observed by Fermi-LAT, which is the regime of interest for identifying the maximum synchrotron photon energies.

2.3. Kinetic Evolution and Radiation Processes

We assume the shock properties are governed solely by the instantaneous Lorentz factor of the flow and model electron acceleration as instantaneous. The accelerated electrons are then advected downstream to radiate. Once electrons are injected into the radiative zone, the evolution is governed by the continuity equation

$$\frac{\partial N'(\gamma, t')}{\partial t'} = \frac{\partial}{\partial \gamma} [\dot{\gamma}'_{\text{cool}} N'(\gamma, t')] + Q'_{\text{inj}}(\gamma, t') - \frac{N'(\gamma, t')}{t'_{\text{esc}}}, \quad (26)$$

where $N'(\gamma, t') = V' n'(\gamma, t')$ is the volume-integrated particle distribution in the comoving frame with the comoving volume V' given by Equation (25), and the escape timescale t'_{esc} is given by Equation (24). The total cooling rate is

$$\dot{\gamma}'_{\text{cool}} = \dot{\gamma}'_{\text{syn}} + \dot{\gamma}'_{\text{KN}} + \dot{\gamma}'_{\text{ad}}, \quad (27)$$

including synchrotron losses, SSC losses with KN corrections, and adiabatic cooling, respectively. We adopt the adiabatic loss term from T. Pennanen et al. (2014),

$$\dot{\gamma}'_{\text{ad}} = -\frac{3\gamma}{5t'}, \quad (28)$$

which is appropriate for a constant-density ISM during the deceleration phase. The injection term Q'_{inj} represents the volume-integrated particle distribution of freshly accelerated electrons. The injected electron spectrum is assumed to follow a power law between γ_{\min} and

γ_{\max} , as defined in Section 2.1, with ε_e entering the spectral modeling only through γ_{\min} . Its normalization is set by the number of particles swept by the shock, given by the comoving particle flux $\Gamma n c$ through an area $\pi(r/\Gamma)^2$, such that

$$\int_1^\infty Q'(\gamma, t') d\gamma = \Gamma n c \pi \left(\frac{r}{\Gamma} \right)^2 = \Gamma n \pi t'^2 c^3. \quad (29)$$

By formulating the problem in terms of the volume-integrated continuity equation, the effects of adiabatic dilution are naturally incorporated. An equivalent description can be obtained by introducing an effective escape term with a timescale comparable to the dynamical expansion time (T. Pennanen et al. 2014; E. Aguilar-Ruiz et al. 2025), which is similar to our choice of t'_{esc} .

The numerical calculations are performed using the code TLECO (Z. Davis et al. 2024), a one-zone model¹² that self-consistently evolves the particle distribution $N(\gamma, t')$ and computes the resulting synchrotron and SSC emission, including KN correction. To evaluate the synchrotron photon energy density relevant for SSC emission, we adopt a photon escape length equal to Δ' , reflecting the thin-shell geometry of the emitting region. All physical ingredients required to evolve the particle spectrum and compute the radiative output have now been specified. We neglect internal γ - γ absorption, as it primarily affects the VHE tail of the SSC component and is not central to our analysis.

The approximation of the Blandford–McKee solution by a one-zone model is not unique, and different choices for the effective emission region and characteristic timescales may introduce order of unity variations. However, such differences do not affect the qualitative behavior or the main conclusions of this work. We have verified that, when adopting identical assumptions and configurations, our numerical implementation reproduces the results of T. Pennanen et al. (2014).

3. FAVORED BURST PARAMETERS

The maximum electron energy manifests as an exponential cutoff in the GRB afterglow spectrum, as given by Equation (20). Although this feature can be intrinsically sharp, it is often dominated by the rising SSC component, resulting in an apparent smooth spectral hardening. In such cases, the observed turnover provides only a lower bound on the maximum synchrotron frequency, yielding a weak constraint on particle acceleration. A significant detection of the exponential cutoff is possible only when it is not obscured by the SSC emission.

¹² The model assumes an isotropic distribution of particles with no spatial dependence.

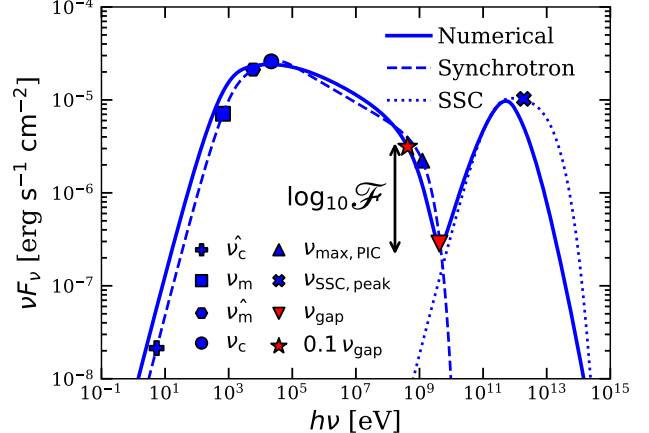


Figure 1. Afterglow spectrum for a burst placed at $D_L = 100$ Mpc at $T_{\text{obs}} = 100$ s. The burst parameters are $\varepsilon_e = 0.1$, $\varepsilon_B = 3.5 \times 10^{-3}$, $E_{\text{iso}} = 10^{54}$ erg, $\Gamma_0 = 500$, $n = 0.5 \text{ cm}^{-3}$, and $p = 2.4$. The solid curve shows the numerical spectrum, while the dashed and dotted curves show the analytical synchrotron and SSC components with characteristic frequencies denoted by blue symbols. The red markers indicate ν_{gap} and $0.1 \nu_{\text{gap}}$, with their vertical separation corresponding to $\log_{10} \mathcal{F}$, which quantifies the prominence of the synchrotron cutoff.

sion. In this section, we investigate the regions of GRB parameter space that favor a clear cutoff. All results presented in this section assume the PIC-motivated acceleration prescription for the synchrotron cutoff. For comparison, under the Bohm prescription the cutoff typically appears at much higher energies, where the emission is already dominated by the SSC component and is therefore rarely observable.

To quantify the cutoff feature, we define a flux ratio \mathcal{F} designed to identify an exponential synchrotron drop, as opposed to a simple power-law decline, in observed spectra. We define

$$\mathcal{F} = \frac{\nu F_\nu(0.1 \nu_{\text{gap}})}{\nu F_\nu(\nu_{\text{gap}})}, \quad (30)$$

where ν_{gap} is the frequency at which νF_ν reaches its local minimum between the synchrotron and SSC peaks, marking the transition from synchrotron-dominated to SSC-dominated emission.

As an illustration, Figure 1 shows an example afterglow spectrum from our numerical calculations. For comparison, we also plot the analytical synchrotron and SSC components following C. Pellouin & F. Daigne (2024), along with the relevant characteristic frequencies, which are provided in Appendix A. The numerical results are in good agreement with the analytical expectations. In the figure, the red ∇ marks the location of ν_{gap} and the red star denotes $0.1 \nu_{\text{gap}}$, with their vertical separation on the logarithmic scale corresponding to $\log_{10} \mathcal{F}$. The ratio \mathcal{F} therefore measures

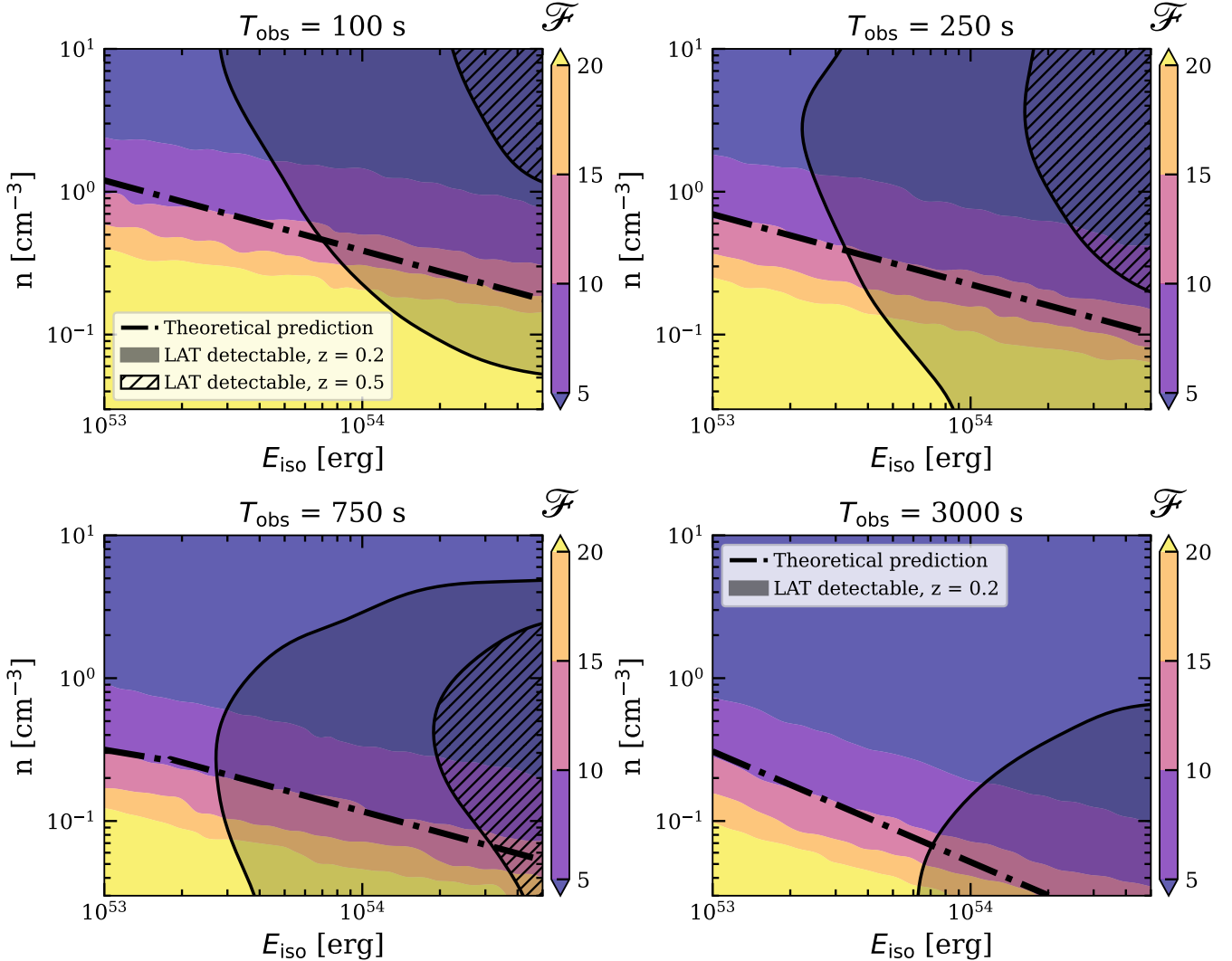


Figure 2. Flux ratio $\mathcal{F} \equiv \nu F_\nu(0.1 \nu_{\text{gap}}) / \nu F_\nu(\nu_{\text{gap}})$ shown as a function of E_{iso} and n at observer times $T_{\text{obs}} = 100, 250, 750$ and 3000 s after trigger. Colors indicate the value of \mathcal{F} , as shown by the color bar. All results are computed using the PIC-motivated acceleration prescription with $\varepsilon_e = 0.1$, $\varepsilon_B = 3.5 \times 10^{-3}$, and $p = 2.4$. Dash-dotted curves denote the theoretical prediction corresponding to $\mathcal{F} = 10$, in good agreement with the numerical results. The shaded and dashed contours indicate detectability for bursts placed at redshifts $z = 0.2$ and $z = 0.5$, respectively.

the effective spectral steepening immediately below the SSC-dominated regime, and becomes large when the synchrotron cutoff occurs well before the SSC component rises. Throughout, we adopt $\mathcal{F} > 10$ as a practical criterion for a detectable exponential drop. For a pure synchrotron spectrum, the steepest physically relevant power-law decline is $\nu F_\nu \propto \nu^{(2-p)/2}$ (R. Sari et al. 1998), which would require $p > 4$ to reproduce $\mathcal{F} > 10$ and is far steeper than expected from both theoretical considerations and observational constraints (P. A. Curran et al. 2010).

Figure 2 shows \mathcal{F} as a function of E_{iso} and n at several observer times. Motivated by PIC simulations, we

fix $\varepsilon_e = 0.1$, $\varepsilon_B = 3.5 \times 10^{-3}$, and $p = 2.4^{13}$, and explore a parameter range representative of GRB afterglows, $10^{53} \text{ erg} < E_{\text{iso}} < 5 \times 10^{54} \text{ erg}$ and $0.03 \text{ cm}^{-3} < n < 10 \text{ cm}^{-3}$ (X.-G. Wang et al. 2018; M. D. Aksulu et al. 2022; A. Rouco Escorial et al. 2023). We find that a large \mathcal{F} , corresponding to a more prominent synchrotron cutoff, is favored for low-energy explosions in low-density environments at early times. To further clarify the parameter dependence, we derive an analytic estimate

$$\mathcal{F} \simeq 2.2 \varepsilon_{e,-1}^{1.3} \varepsilon_{B,-2.5}^{-0.1} E_{\text{iso},54}^{-0.78} n_0^{-1.6} T_{\text{obs},2}^{-0.95}, \quad (31)$$

¹³ We fix the initial Lorentz factor $\Gamma_0 = 500$, which has negligible impact as the blast wave enters the deceleration phase rapidly.

evaluated for $p \simeq 2.4$ at $T_{\text{obs}} \simeq 100$ s with $E_{\text{iso}} \sim 10^{54}$ erg and $n \sim 1 \text{ cm}^{-3}$. Expressions applicable to other parameter regimes and observer times, along with a detailed derivation, are given in Appendix B. The dash-dotted curves in Figure 2 show the corresponding theoretical prediction for $\mathcal{F} = 10$ at different observer times, in good agreement with the numerical results.

Although low-energy bursts in low-density environments show a clear exponential cutoff, they may be intrinsically faint and therefore difficult to detect, depending on their distance. We therefore assess the detectability across the parameter space. Since $h\nu_{\text{max}} \sim \text{GeV}$, Fermi-LAT is well suited to probe this regime. A detailed prediction of detectability for a given spectral shape is highly instrument- and case-dependent and thus beyond the scope of this work. Instead, we estimate detectability using the observed cumulative fluence at $0.1\nu_{\text{gap}}$ and evaluate the corresponding signal-to-noise ratio (SNR)¹⁴. We require $\text{SNR} > 5$ as a detection threshold. This criterion is conservative, as many LAT-detected GRB afterglows fall below this threshold.

The opaque and dashed contours in Figure 2 indicate the detectability for bursts placed at redshifts $z = 0.2$ and $z = 0.5$, respectively. At early times, the detectable parameter space expands as $0.1\nu_{\text{gap}}$ shifts to lower energies within the LAT band during deceleration, increasing the accumulated photon counts. At later times, detectability becomes increasingly limited by background noise as exposure time grows. Consequently, the optimal window for identifying the exponential cutoff lies at times of a few hundred seconds. For $z = 0.2$, there is substantial overlap between detectable events and those exhibiting clear spectral cutoff even at ~ 3000 s, while for $z = 0.5$ the overlap is significantly reduced. The successful detection of a clear spectral cutoff relies on a GRB that satisfies several favorable conditions.

4. OBSERVATIONS

Motivated by the results of the previous section, we focus on two well-studied GRB afterglows with early-time Fermi-LAT detections: GRB 190114C and GRB 130427A. We utilize multiwavelength data to model their early-time broadband spectra, adopting parameter ranges motivated by both PIC simulations and GRB observations. As discussed in Section 2.1, we fix

¹⁴ We adopt the Fermi-LAT instrument response functions from https://www.slac.stanford.edu/exp/glast/groups/canda/lat_Performance.htm with the mode of P8R3_SOURCE_V3. Only Poisson and background noise are considered, with the background noise model taken from https://fermi.gsfc.nasa.gov/ssc/data/analysis/software/aux/iso_P8R3_SOURCE_V3_v1.txt.

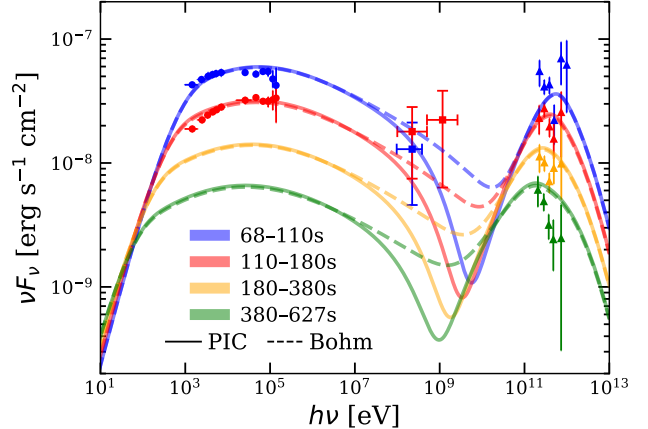


Figure 3. Spectral fitting of GRB 190114C from X-ray to TeV energies across multiple observation intervals. Different colors denote different time intervals, as indicated in the legend. Circles, squares, and triangles represent data from Swift/XRT-BAT, Fermi-LAT, and MAGIC, respectively, with error bars indicating 1σ uncertainties. Solid curves are based on the PIC acceleration model, while dashed curves correspond to the Bohm diffusion limit. Both of them adopt $\varepsilon_e = 0.1$, $\varepsilon_B = 10^{-3}$, $E_{\text{iso}} = 1.5 \times 10^{54}$ erg, $n = 1 \text{ cm}^{-3}$, $p = 2.4$, and $\Gamma_0 = 500$.

$\varepsilon_e = 0.1$ and $p \simeq 2.4$, while allowing $10^{-4} \lesssim \varepsilon_B \leq 5 \times 10^{-3}$. For GRB observations, the isotropic-equivalent prompt energy $E_{\gamma,\text{iso}}$ is typically well constrained. For small values of ε_B ($\sim 10^{-4}$ to 10^{-3}), the radiative efficiency is inferred to be $E_{\gamma,\text{iso}}/E_{\text{iso}} \simeq 20\%$ (P. Beniamini et al. 2016). We therefore adopt $E_{\text{iso}} = 5E_{\gamma,\text{iso}}$ and treat the ambient density n as a free parameter. We also fix the initial bulk Lorentz factor to $\Gamma_0 = 500$, noting that our results are insensitive to this choice provided that the jet has entered the deceleration phase by the time the spectrum is observed.

4.1. GRB 190114C

GRB 190114C was a bright long GRB with an isotropic-equivalent gamma-ray energy of $E_{\gamma,\text{iso}} \simeq 3 \times 10^{53}$ erg at $z = 0.42$ (M. Ajello et al. 2020). Its relatively low redshift enabled extensive multiwavelength follow-up observations. Shortly after the trigger, the MAGIC Cherenkov telescopes detected VHE emission, marking the first unambiguous detection of TeV photons from a GRB and inaugurating ground-based VHE afterglow studies (V. A. Acciari et al. 2019b).

Here we adopt the spectral energy distribution presented in V. A. Acciari et al. (2019a) and focus on the first four MAGIC time intervals. The multiwavelength observations, including Swift/XRT-BAT and Fermi/GBM data, are summarized in Figure 3, with different colors denoting the corresponding time intervals. The analyzed spectra span from $T_0 + 68$ s to $T_0 + 625$ s, where T_0 marks the onset of the prompt emission. The

active prompt phase lasts for approximately 25 s, ensuring that the selected time window is minimally contaminated by prompt emission.

During the first time interval (68–110 s; blue points), the Swift/XRT–BAT observations indicate that the synchrotron component peaks in the X-ray band. At higher energies, up to $\lesssim 1\text{GeV}$, the spectrum declines with energy, consistent with the Fermi-LAT measurements. At even higher energies, the MAGIC detection above 0.2 TeV reveals a spectral hardening attributed to SSC emission. However, the locations of the spectral maximum and minimum remain poorly constrained owing to the limited coverage between the X-ray and TeV bands. A simultaneous broadband fit is therefore required to better constrain the maximum synchrotron frequency.

Within the parameter ranges discussed above, a reasonable fit to the spectrum in Figure 3 yields $\varepsilon_B = 10^{-3}$, $E_{\text{iso}} = 1.5 \times 10^{54} \text{ erg}$, $n = 1 \text{ cm}^{-3}$, and $p = 2.4$. The resulting model reproduces the observed spectrum over many orders of magnitude in photon energy and follows the observed temporal evolution, demonstrating the overall consistency of our framework. However, uncertainties in the Fermi-LAT measurements limit our ability to distinguish between the PIC acceleration model and the Bohm diffusion limit, as both yield similar spectral shapes for the same parameter set. The primary difference lies in the depth of the gap between the synchrotron and SSC components, but it is difficult to resolve owing to limited photon statistics at early times for this burst. A clearer detection of an exponential cutoff would likely be achievable if the LAT were not occulted by Earth and could maintain coverage up to $\sim T_0 + 625 \text{ s}$ (M. Ajello et al. 2020). Nevertheless, the presence of TeV observations plays a crucial role in reducing degeneracies in broadband spectral modeling.

4.2. GRB 130427A

GRB 130427A is the second brightest long GRB observed to date, with an isotropic-equivalent gamma-ray energy of $E_{\gamma,\text{iso}} \simeq 8 \times 10^{53} \text{ erg}$ at a redshift of $z = 0.34$. A rich multiwavelength data set is available for this event, although it was not observed by MAGIC. Here we adopt the Fermi-LAT spectral energy distribution from M. Ackermann et al. (2014) and focus on the interval from $T_0 + 138 \text{ s}$ to $T_0 + 750 \text{ s}$, which provides sufficiently early coverage while maintaining good data quality. We adopt the Swift/XRT spectrum from R. Ruffini et al. (2015) for the same time interval¹⁵. All observa-

¹⁵ The spectral data in R. Ruffini et al. (2015) cover the interval from $T_0 + 196 \text{ s}$ to $T_0 + 750 \text{ s}$. To extend the spectrum to earlier times ($T_0 + 138$ to $T_0 + 196 \text{ s}$), we approximate the emission us-

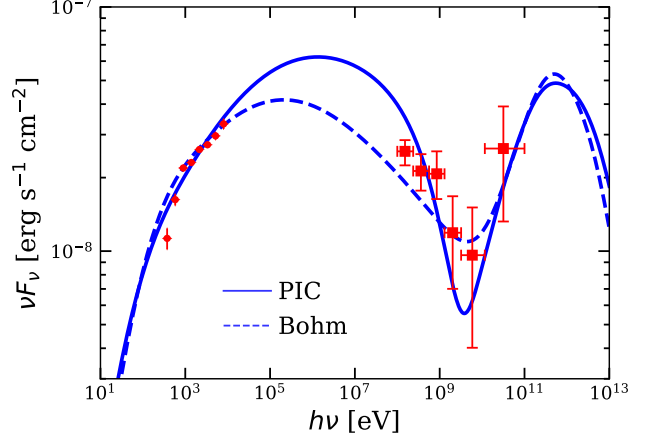


Figure 4. Spectral fitting of GRB 130427A from X-ray to GeV energies over the interval 138–750 s after the onset of the prompt emission. Circles and squares denote data from Swift/XRT and Fermi-LAT, respectively, with error bars indicating 1σ uncertainties. The solid curve shows the PIC-motivated acceleration model, while the dashed curve corresponds to the Bohm diffusion limit. Both models adopt $\varepsilon_e = 0.1$, $\varepsilon_B = 3 \times 10^{-4}$, $E_{\text{iso}} = 4 \times 10^{54} \text{ erg}$, and $\Gamma_0 = 500$. The PIC model assumes $n = 1.5 \text{ cm}^{-3}$ and $p = 2.2$, whereas the Bohm model adopts $n = 1 \text{ cm}^{-3}$ and $p = 2.4$.

tional data are summarized in Figure 4. The definition of T_{90} for GRB 130427A is somewhat ambiguous, but the prompt emission is dominated by an initial pulse complex lasting approximately 18 s. Our selected time window is therefore not significantly contaminated by prompt emission.

Fortunately, Fermi-LAT continued to detect the burst up to $T_0 + 750 \text{ s}$, allowing sufficient photon statistics to reveal spectral hardening associated with SSC emission. The minimum of the spectral energy distribution, ν_{gap} , occurs at energies of a few GeV, although its exact location is limited by photon statistics and background noise. We therefore perform a simultaneous broadband fit to fully exploit the available data and to place better constraints on ν_{max} .

A reasonable fit to the spectrum in Figure 4, within the parameter ranges discussed above, yields $\varepsilon_B = 3 \times 10^{-4}$ and $E_{\text{iso}} = 4 \times 10^{54} \text{ erg}$. For the PIC model, the best-fit parameters are $n = 1.5 \text{ cm}^{-3}$ and $p = 2.2$, while the Bohm limit favors $n = 1 \text{ cm}^{-3}$ and $p = 2.4$. Both acceleration prescriptions provide comparably good descriptions of the observed spectrum. Although the Fermi-LAT data for GRB 130427A provide improved constraints compared to GRB 190114C and

ing the XRT light curve and photon index available from the Swift/XRT repository. We verify that the spectrum is dominated by emission from $T_0 + 196$ to $T_0 + 750 \text{ s}$, ensuring that this approximation does not affect our results.

suggest a possible spectral turnover at a few GeV, the uncertainties remain too large to discriminate between the PIC and Bohm acceleration scenarios.

Overall, while the data suggest a spectral drop followed by hardening, the uncertainties remain sufficiently large that even a single power-law spectrum in the Fermi-LAT band cannot be ruled out. An exponential cutoff could become detectable if the burst were closer by a factor of a few. Moreover, the lack of MeV band coverage introduces degeneracies in spectral modeling, highlighting the importance of future observations that bridge this energy range.

5. CONCLUSION AND DISCUSSION

In this Letter, we investigate particle acceleration models in weakly magnetized relativistic collisionless shocks and apply them to GRB afterglows to place observational constraints on acceleration physics. We model the GRB afterglow spectrum and its temporal evolution during the relativistic deceleration phase. The primary observational diagnostic of the acceleration process is the synchrotron cutoff, which encodes the maximum attainable energy of accelerated electrons and thus the acceleration rate. A significant cutoff is expected only when the SSC component does not dominate near the maximum synchrotron frequency. We quantify the prominence of the cutoff using the flux ratio \mathcal{F} , with larger values corresponding to weaker SSC strength. Exploring a parameter space motivated by GRB observations and PIC simulations, we find that low-energy bursts in low-density environments exhibit a pronounced exponential cutoff at early times. The behavior is in good agreement with the theoretical prediction of \mathcal{F} given in Equation (31).

The conditions that need to be fulfilled for the detection of a clear exponential cutoff are not commonly satisfied. Low-energy bursts are only detectable at smaller distances, whereas early afterglow phases may be missed by Fermi-LAT owing to instrumental constraints. We examine two well-studied events, GRB 190114C and GRB 130427A, and find that the available LAT data are insufficient to robustly discriminate between PIC-motivated acceleration and the theoretical Bohm limit, while the broadband spectral modeling suffers from significant degeneracies. Future TeV observations with the Cherenkov Telescope Array Observatory (W. Hofmann & R. Zanin 2023) and MeV coverage from upcoming or proposed missions such as COSI (J. Tomsick et al. 2024) and AMEGO-X (R. Caputo et al. 2022) will be essential to break degeneracies.

The burst properties favored for detecting a clear exponential cutoff, namely low circumburst densities and

small kinetic energies, naturally point to short GRBs. An example well suited for our purpose is GRB 160821B, one of the closest short GRBs known, at $z = 0.162$ with $E_{\gamma, \text{iso}} \sim 1.2 \times 10^{49}$ erg (V. A. Acciari et al. 2021). Afterglow modeling indicates $E_{\text{iso}} \sim 10^{50}$ erg and $n \approx 10^{-3} \text{ cm}^{-3}$ (E. Troja et al. 2019), conditions favorable for detecting an exponential synchrotron cutoff. Unfortunately, the burst lay near the edge of the Fermi-LAT field of view during the early interval because the spacecraft had repointed toward GRB 160821A (F. Longo et al. 2016a,b). LAT coverage resumed only at $T_0 + 5285$ s, and no detection was recorded. MAGIC observations were likewise hampered by poor atmospheric conditions and moonlight, yielding at most a low-significance excess (V. A. Acciari et al. 2021).

GRB 221009A (the BOAT; E. Burns et al. 2023) provides a notable counterexample. The burst saturated the LAT at early times, and once nominal operations resumed it remained within the field of view only briefly at ~ 120 s, before re-entering at $\sim T_0 + 4000$ s (M. Axelsson et al. 2025), which has been outside our time window of interest. During this early valid interval, the photon index was already < 2 (M. Axelsson et al. 2025), indicating that the LAT band was dominated by SSC emission and consistent with the event's extreme energetics. These considerations motivate excluding GRB 221009A from our main analysis, while its rapid SSC evolution may warrant a dedicated future study.

Recent PIC simulations (D. Grošelj et al. 2024) reveal that the post-shock magnetic field is highly intermittent, with $\sim 1\%$ of the volume containing $\sim 50\%$ of the magnetic energy. This picture deviates from the commonly assumed uniform magnetic field strength throughout the shocked region and can affect both synchrotron and SSC emission. The long-term evolution of the magnetic field downstream of the shock may also play an important role. The PIC-simulation prescription for particle acceleration adopted here assumes a vanishingly small upstream magnetization. If this is not the case, the maximum particle energy may instead be limited by the influence of the large-scale ambient field, potentially shifting the synchrotron cutoff to lower energies (e.g., L. Sironi et al. 2013; B. Reville & A. R. Bell 2014; I. Plotnikov et al. 2018; Z.-Q. Huang et al. 2022). In addition, our analysis neglects the jet angular structure (e.g., T. E. Jacovich et al. 2021; H. Wang et al. 2024), possible reprocessing of the ambient medium by gamma-ray photons (A. M. Beloborodov 2002; E. V. Derishev & T. Piran 2016; D. Grošelj et al. 2022; R. Golant et al. 2025), and variations in the ambient density (e.g., P. Mimica & D. Giannios 2011). Accounting for these effects represents important directions for future work.

ACKNOWLEDGMENTS

We thank Zachary Davis for assistance with the TLECO code. Z. W. and D. Giannios acknowledge support from the NSF AST-2308090 and AST-2510569 grants. PB is supported by a grant from the National Aeronautics and Space Administration (NASA 80NSSC24K0770), by a grant (no. 2024788) from the United States-Israel Binational Science Foundation (BSF), Jerusalem, Israel and by a grant (no. 1649/23) from the Israel Science Foundation. D. Grošelj is supported by the Research Foundation—Flanders (FWO) Senior Postdoctoral Fellowship 12B1424N. L.S. acknowledges support from DoE Early Career Award DE-SC0023015, NASA

ATP 80NSSC24K1238, NASA ATP 80NSSC24K1826, and NSF AST-2307202. This research was facilitated by the Multimessenger Plasma Physics Center (MPPC) NSF grant PHY-2206609 to L.S., and by a grant from the Simons Foundation (MP-SCMPS-0000147, to L.S.). This research has made use of NASA’s Astrophysics Data System Bibliographic Services.

Facilities: Fermi(LAT), Swift(XRT and BAT), MAGIC

Software: SciPy (P. Virtanen et al. 2020), NUMPY (C. R. Harris et al. 2020), MATPLOTLIB (J. D. Hunter 2007), TLECO (Z. Davis et al. 2024)

APPENDIX

A. CHARACTERISTIC BREAKS AND ANALYTICAL SPECTRA

In this section, we derive the characteristic frequencies of the afterglow spectrum and their dependence on the burst parameters. All critical Lorentz factors of the electron energy distribution are unprimed and defined in the shocked fluid frame, while all characteristic frequencies are given in the observer frame with $z = 0$.

Using the Blandford–McKee self-similar solution (R. D. Blandford & C. F. McKee 1976) and the definition of the observer timescale in Equation (18), the bulk Lorentz factor of the shocked fluid can be written as

$$\Gamma \simeq 200 E_{\text{iso},54}^{1/8} n_0^{-1/8} T_{\text{obs},2}^{-3/8} \quad (\text{A1})$$

The minimum electron Lorentz factor given in Equation (2) then becomes

$$\gamma_{\text{min}} \simeq 3.5 \times 10^4 \left(\frac{p-2}{p-1} \right) \varepsilon_{e,-1} E_{\text{iso},54}^{1/8} n_0^{-1/8} T_{\text{obs},2}^{-3/8} \quad (\text{A2})$$

where $\varepsilon_e = 0.1, \varepsilon_{e,-1}$. The corresponding characteristic synchrotron frequency is

$$h\nu_m \simeq 10^4 \left(\frac{p-2}{p-1} \right)^2 \varepsilon_{e,-1}^2 \varepsilon_{B,-2.5}^{1/2} E_{\text{iso},54}^{1/2} T_{\text{obs},2}^{-3/2} \text{ eV} \quad (\text{A3})$$

Another important Lorentz factor is the synchrotron cooling Lorentz factor γ_c^{syn} , defined by equating the synchrotron cooling timescale to the effective cooling timescale, $\gamma_c^{\text{syn}} = \dot{\gamma}_c^{\text{syn}} t'_{\text{cool}}$. The effective cooling timescale accounts for both particle escape (t'_{esc}) and adiabatic expansion (t'_{ad}) timescales. Following E. Aguilar-Ruiz et al. (2025), the adiabatic timescale is

$$\frac{1}{t'_{\text{ad}}} = \frac{3\Gamma\beta c}{r} \left(1 - \frac{1}{3} \frac{d \log \Gamma}{d \log r} \right) = \frac{9\Gamma c}{2r}. \quad (\text{A4})$$

Together with the escape time t'_{esc} (Equation (24)), the effective cooling timescale is

$$t'_{\text{cool}} = \left(\frac{1}{t'_{\text{esc}}} + \frac{1}{t'_{\text{ad}}} \right)^{-1} = \frac{6r}{59\Gamma c} \simeq 0.1 \frac{r}{\Gamma c}. \quad (\text{A5})$$

The synchrotron cooling Lorentz factor is then

$$\gamma_c^{\text{syn}} = \frac{6\pi m_e c}{\sigma_T B'^2 t'_{\text{cool}}} = 4 \times 10^4 \varepsilon_{B,-2.5}^{-1} E_{\text{iso},54}^{-3/8} n_0^{-5/8} T_{\text{obs},2}^{1/8} \quad (\text{A6})$$

with the associated cooling frequency

$$h\nu_c^{\text{syn}} = 1.3 \times 10^4 \varepsilon_{B,-2.5}^{-3/2} E_{\text{iso},54}^{-1/2} n_0^{-1} T_{\text{obs},2}^{-1/2} \text{ eV} \quad (\text{A7})$$

For most of the parameter space considered here, Klein–Nishina effects cannot be neglected, and the inverse-Compton cooling rate becomes energy dependent. As a result, the Compton Y parameter depends on the energy of the scattered electrons. The total cooling break should include the contribution from SSC losses and is determined by

$$\gamma_c [1 + Y(\gamma_c)] = \gamma_c^{\text{syn}}, \nu_c [1 + Y(\gamma_c)]^2 = \nu_c^{\text{syn}}, \quad (\text{A8})$$

where $Y(\gamma_c)$ is the Compton parameter evaluated at γ_c . $Y(\gamma_c)$ can be obtained iteratively following [C. Pellouin & F. Daigne \(2024\)](#), or estimated using the approach of [E. Nakar et al. \(2009\)](#) with details provided in Appendix B. For the parameter space relevant to this work, $Y(\gamma_c)$ is modest or low ($Y(\gamma_c) \lesssim 1$), so that $\nu_c > \nu_m$ remains satisfied. In this regime, the synchrotron νF_ν^{syn} spectrum peaks at ν_c , while the peak of the F_ν^{syn} spectrum occurs at ν_m and can be estimated following [R. Sari et al. \(1998\)](#),

$$F_{\nu',\text{peak}}^{\text{syn}} = \frac{\Gamma N P'_{\nu',\text{peak}}}{4\pi D_L^2} \quad (\text{A9})$$

where D_L is the luminosity distance, N is the total number of particles swept by the equivalent spherical blast wave, and the peak spectral power per electron in the comoving frame is

$$P'_{\nu',\text{peak}} = \frac{\sqrt{3}e^3 B'}{m_e c^2}. \quad (\text{A10})$$

Following [E. Nakar et al. \(2009\)](#) and [C. Pellouin & F. Daigne \(2024\)](#), we approximate the inverse-Compton cross section by assuming that scattering is fully suppressed in the KN regime. Under this assumption, a synchrotron photon emitted by an electron of Lorentz factor γ can be upscattered only by electrons with Lorentz factors below a critical value $\hat{\gamma}$, such that scattering remains in the Thomson regime,

$$\hat{\gamma} = \frac{w_{\text{KN}} \Gamma m_e c^2}{h\nu(\gamma)}. \quad (\text{A11})$$

where we adopt $w_{\text{KN}} = 0.2$ following [S. Yamasaki & T. Piran \(2022\)](#). The corresponding characteristic KN breaks are

$$\hat{\gamma}_m = \frac{w_{\text{KN}} \Gamma m_e c^2}{h\nu_m} = 2 \times 10^3 \left(\frac{p-1}{p-2} \right)^2 \varepsilon_{e,-1}^{-2} \varepsilon_{B,-2.5}^{-1/2} E_{\text{iso},54}^{-3/8} n_0^{-1/8} T_{\text{obs},2}^{9/8}, \quad (\text{A12})$$

and

$$\hat{\gamma}_c = \frac{w_{\text{KN}} \Gamma m_e c^2}{h\nu_c} [1 + Y(\gamma_c)]^2 = 1.6 \times 10^3 [1 + Y(\gamma_c)]^2 \varepsilon_{B,-2.5}^{3/2} E_{\text{iso},54}^{5/8} n_0^{7/8} T_{\text{obs},2}^{1/8}. \quad (\text{A13})$$

Given these characteristic breaks, the SSC spectrum can be constructed following the prescription of [C. Pellouin & F. Daigne \(2024\)](#). The synchrotron and SSC spectra shown in Figure 1 correspond to Case S4 in [C. Pellouin & F. Daigne \(2024\)](#)¹⁶.

B. DERIVATION AND DISCUSSION OF \mathcal{F}

Here we derive the analytical approximation for \mathcal{F} given in Equation (31). As discussed in Section 3, values of $\mathcal{F} \gtrsim 10$ cannot be produced by a pure synchrotron power-law spectrum and therefore require a contribution from the synchrotron cutoff. This implies that the spectral minimum ν_{gap} must be greater than the cutoff frequency ν_{max} . If $0.1\nu_{\text{gap}} > \nu_{\text{max}}$, \mathcal{F} would probe only the exponential decay and become very large. We neglect this case, as the SSC contribution is negligible and the cutoff is always clear. We therefore focus on the regime $0.1\nu_{\text{gap}} < \nu_{\text{max}} < \nu_{\text{gap}}$.

In this regime, the power-law decline of the synchrotron spectrum is subdominant compared to the exponential cutoff, and the flux ratio is dominated by the cutoff contribution. We thus approximate

$$\nu F_\nu(0.1\nu_{\text{gap}}) \approx \nu F_\nu(\nu_{\text{max}}) \approx \nu F_\nu^{\text{syn}}(\nu_{\text{max}}). \quad (\text{B14})$$

using the fact that the emission at ν_{max} is synchrotron dominated since $\nu_{\text{max}} < \nu_{\text{gap}}$.

¹⁶ The spectral slope between γ_m and γ_c should be p , and the value quoted in the original reference is a typo.

At ν_{gap} , the synchrotron and SSC components become comparable, so that

$$\nu F_\nu(\nu_{\text{gap}}) \approx \nu F_\nu^{\text{IC}}(\nu_{\text{gap}}) \quad (\text{B15})$$

Moreover, because the power-law rise in the SSC spectrum is insignificant compared to the exponential drop, we can further approximate

$$\nu F_\nu^{\text{IC}}(\nu_{\text{gap}}) \approx \nu F_\nu^{\text{IC}}(\nu_{\text{max}}) \quad (\text{B16})$$

Combining these relations, we arrive at the following approximation for \mathcal{F} :

$$\mathcal{F} = \frac{\nu F_\nu(0.1\nu_{\text{gap}})}{\nu F_\nu(\nu_{\text{gap}})} \approx \frac{\nu F_\nu^{\text{syn}}(\nu_{\text{max}})}{\nu F_\nu^{\text{IC}}(\nu_{\text{max}})}. \quad (\text{B17})$$

With these approximations, \mathcal{F} reduces to the ratio of the synchrotron and SSC amplitudes of νF_ν evaluated at ν_{max} . To estimate the relative normalization of the two components, the Compton parameter naturally enters. In particular,

$$Y(\gamma_c) = \frac{\nu F_\nu(\nu_{\text{peak}}^{\text{IC}})}{\nu F_\nu(\nu_c)} \simeq \frac{\nu F_\nu^{\text{IC}}(\nu_{\text{peak}}^{\text{IC}})}{\nu F_\nu^{\text{syn}}(\nu_c)} \quad (\text{B18})$$

where we have used the fact that, for the parameter space of interest, the synchrotron peak occurs at $\nu_{\text{peak}}^{\text{syn}} = \nu_c$. Following E. Nakar et al. (2009), the Compton parameter in the slow-cooling regime satisfies

$$Y(\gamma_c)[1 + Y(\gamma_c)] \approx \frac{1}{3} \frac{\varepsilon_e}{\varepsilon_B} \left(\frac{\gamma_c}{\gamma_m} \right)^{2-p} \left(\frac{\min\{\gamma_c, \hat{\gamma}_c\}}{\gamma_c} \right)^{\frac{3-p}{2}}. \quad (\text{B19})$$

The prefactor 1/3 accounts for the fact that the borders of the shock fluid expand at a speed of $c/3$ rather than c . Using the expression for γ_c and $\hat{\gamma}_c$ derived in Equation (A8) and Equation (A13), we obtain

$$\frac{\hat{\gamma}_c}{\gamma_c} = 0.04 [1 + Y(\gamma_c)]^3 \varepsilon_{B,-2.5}^{5/2} E_{\text{iso},54} n_0^{3/2}. \quad (\text{B20})$$

Since a clear synchrotron cutoff requires $Y(\gamma_c) \lesssim \mathcal{O}(1)$, we typically have $\gamma_c > \hat{\gamma}_c$ in the regime of interest, where the KN suppression becomes important. Then Equation (B21) reduces to

$$\begin{aligned} Y(\gamma_c) &\approx \frac{1}{3} \frac{\varepsilon_e}{\varepsilon_B} \left(\frac{\gamma_c}{\gamma_m} \right)^{2-p} \left(\frac{\hat{\gamma}_c}{\gamma_c} \right)^{\frac{3-p}{2}} [1 + Y(\gamma_c)]^{-1} \\ &= 13.7 \left(\frac{p-2}{p-1} \right)^{p-2} [1 + Y(\gamma_c)]^{\frac{3-p}{2}} \varepsilon_{e,-1}^{p-1} \varepsilon_{B,-2.5}^{\frac{3-p}{4}} E_{\text{iso},54}^{\frac{1}{2}} n_0^{\frac{5-p}{4}} T_{\text{obs},2}^{-\frac{p-2}{2}}. \end{aligned} \quad (\text{B21})$$

For $p \simeq 2.4$, the strongest dependence is on the circumburst density, and requiring $Y(\gamma_c) \lesssim \mathcal{O}(1)$ implies $n \lesssim 1 \text{ cm}^{-3}$, consistent with the condition $\gamma_c > \hat{\gamma}_c$ assumed above.

Using $Y(\gamma_c)$, we estimate the ratio between $\nu F_\nu^{\text{syn}}(\nu_{\text{max}})$ and $\nu F_\nu^{\text{IC}}(\nu_{\text{max}})$. For $\gamma_c > \hat{\gamma}_c$ and $Y(\gamma_c) \lesssim \mathcal{O}(1)$, the synchrotron spectrum between ν_c and ν_{max} follows the standard power-law decline, $\nu F_\nu \propto \nu^{(2-p)/2}$ (E. Nakar et al. 2009; C. Pelloquin & F. Daigne 2024). Therefore,

$$\begin{aligned} \nu F_\nu^{\text{syn}}(\nu_{\text{max}}) &= \left(\frac{\nu_{\text{max}}}{\nu_c} \right)^{\frac{2-p}{2}} \nu F_\nu^{\text{syn}}(\nu_c) \\ &= \left(\frac{\nu_{\text{max}}}{\nu_c} \right)^{\frac{2-p}{2}} \frac{\nu F_\nu^{\text{IC}}(\nu_{\text{peak}}^{\text{IC}})}{Y(\gamma_c)}, \end{aligned} \quad (\text{B22})$$

where the second equality follows from the definition of the Compton parameter. To relate $\nu F_\nu^{\text{IC}}(\nu_{\text{peak}}^{\text{IC}})$ to $\nu F_\nu^{\text{IC}}(\nu_{\text{max}})$, we next derive the SSC characteristic frequencies in between. The SSC peak frequency is given by (E. Nakar et al. 2009)

$$h\nu_{\text{peak}}^{\text{IC}} = \frac{4}{3} \gamma_c \hat{\gamma}_c \nu_c = 1.1 \times 10^3 [1 + Y(\gamma_c)]^{-1} \varepsilon_{B,-2.5}^{-1} E_{\text{iso},54}^{-1/4} n_0^{-3/4} T_{\text{obs},2}^{-1/4} \text{ GeV}, \quad (\text{B23})$$

while another important SSC break is

$$h\nu_m^{IC} = \frac{4}{3}\gamma_m^2\nu_m = 1.6 \times 10^4 \left(\frac{p-2}{p-1}\right)^4 \varepsilon_{e,-1}^4 \varepsilon_{B,-2.5}^{1/2} E_{iso,54}^{3/4} T_{obs,2}^{-9/4} \text{ GeV.} \quad (B24)$$

For fiducial parameters and $p \simeq 2.4$, we find that $\nu_m^{IC} \simeq 100 \text{ GeV} < \nu_{peak}^{IC}$. Moreover, ν_m^{IC} decreases rapidly with observer time, so the ordering $\nu_m^{IC} < \nu_{peak}^{IC}$ is expected throughout the parameter space and time range of interest. Between ν_m^{IC} and ν_{peak}^{IC} , the SSC spectrum is relatively flat, with $\nu F_\nu^{IC} \propto \nu^{(3-p)/2}$, yielding

$$\nu F_\nu^{IC}(\nu_m^{IC}) = \nu F_\nu^{IC}(\nu_{peak}^{IC}) \left(\frac{\nu_m^{IC}}{\nu_{peak}^{IC}}\right)^{\frac{3-p}{2}}. \quad (B25)$$

From this point onward, we adopt the PIC prescription for the maximum synchrotron frequency. At observer times of a few hundred seconds, the SSC break remains above the synchrotron cutoff,

$$h\nu_{max,PIC} \simeq 0.8 \varepsilon_{B,-2.5}^{-1/6} E_{iso,54}^{1/4} n_0^{-1/12} T_{obs,2}^{-3/4} \text{ GeV.} \quad (B26)$$

Below ν_m^{IC} , the SSC spectrum rises more steeply, following $\nu F_\nu^{IC} \propto \nu^{4/3}$. Consequently,

$$\nu F_\nu^{IC}(\nu_{max,PIC}) = \nu F_\nu^{IC}(\nu_m^{IC}) \left(\frac{\nu_{max,PIC}}{\nu_m^{IC}}\right)^{\frac{4}{3}}. \quad (B27)$$

Between ν_m^{IC} and ν_{peak}^{IC} the SSC spectrum is relatively flat, whereas below ν_m^{IC} it rises much more steeply. As a result, even a modest separation between $\nu_{max,PIC}$ and ν_m^{IC} substantially suppresses $\nu F_\nu^{IC}(\nu_{max,PIC})$ relative to its peak value, making the SSC component subdominant at $\nu_{max,PIC}$ and enhancing the visibility of the synchrotron cutoff. Because $\nu_m^{IC} \propto T_{obs}^{-9/4}$ decreases rapidly with time, it quickly approaches $\nu_{max,PIC}$ and can even fall below it at $T_{obs} \gtrsim 10^3 \text{ s}$. This behavior explains why a clear synchrotron cutoff is strongly favored at early observer times.

If $\nu_{max,PIC} < \nu_m^{IC}$, then using Equations (B22), (B25), and (B27), we obtain

$$\begin{aligned} \frac{\nu F_\nu^{syn}(\nu_{max,PIC})}{\nu F_\nu^{IC}(\nu_{max,PIC})} &= \left(\frac{\nu_{max,PIC}}{\nu_c}\right)^{\frac{2-p}{2}} \frac{\nu F_\nu^{IC}(\nu_{peak}^{IC})}{\nu F_\nu^{IC}(\nu_{max,PIC}) Y(\gamma_c)} \\ &= Y(\gamma_c)^{-1} \left(\frac{\nu_{max,PIC}}{\nu_c}\right)^{\frac{2-p}{2}} \left(\frac{\nu_m^{IC}}{\nu_{peak}^{IC}}\right)^{\frac{p-3}{2}} \left(\frac{\nu_{max,PIC}}{\nu_m^{IC}}\right)^{-\frac{4}{3}}. \end{aligned} \quad (B28)$$

Combining the above expression with Equations (B17) and (B21), the flux ratio can be written as

$$\begin{aligned} \mathcal{F} &\approx \frac{\nu F_\nu^{syn}(\nu_{max,PIC})}{\nu F_\nu^{IC}(\nu_{max,PIC})} \\ &= Y(\gamma_c)^{-1} \left(\frac{\nu_{max,PIC}}{\nu_c}\right)^{\frac{2-p}{2}} \left(\frac{\nu_m^{IC}}{\nu_{peak}^{IC}}\right)^{\frac{p-3}{2}} \left(\frac{\nu_{max,PIC}}{\nu_m^{IC}}\right)^{-\frac{4}{3}} \\ &= 4 \times 10^7 (4 \times 10^3)^{-\frac{p}{2}} \left(\frac{p-2}{p-1}\right)^{\frac{4}{3}+p} [1 + Y(\gamma_c)]^{-1} \varepsilon_{e,-1}^{p+\frac{1}{3}} \varepsilon_{B,-2.5}^{\frac{3p-7}{9}} E_{iso,54}^{\frac{p}{8}-\frac{7}{12}} n_0^{\frac{p}{6}-\frac{97}{72}} T_{obs,2}^{-\frac{3p+2}{8}}. \end{aligned} \quad (B29)$$

Equation (B21) can be used for a quick estimate of $Y(\gamma_c)$. For $Y(\gamma_c) < 1$, we have $(1 + Y) \simeq 1$, while for $Y(\gamma_c) \gtrsim 1$, $(1 + Y(\gamma_c)) \sim Y(\gamma_c)$ while the Compton parameter is still expected to be of order unity. In this latter case, we may further approximate $[1 + Y(\gamma_c)]^{(3-p)/2} \simeq 1$ since the exponent $(3-p)/2$ is small for $p \simeq 2.4$. The resulting expressions for \mathcal{F} are therefore

$$\mathcal{F} \simeq \begin{cases} 4 \times 10^7 (4 \times 10^3)^{-\frac{p}{2}} \left(\frac{p-2}{p-1}\right)^{\frac{4}{3}+p} \varepsilon_{e,-1}^{p+\frac{1}{3}} \varepsilon_{B,-2.5}^{\frac{3p-7}{9}} E_{iso,54}^{\frac{p}{8}-\frac{7}{12}} n_0^{\frac{p}{6}-\frac{97}{72}} T_{obs,2}^{-\frac{3p+2}{8}} & \text{for } Y(\gamma_c) < 1 \\ 3 \times 10^6 (4 \times 10^3)^{-\frac{p}{2}} \left(\frac{p-2}{p-1}\right)^{\frac{10}{3}} \varepsilon_{e,-1}^{\frac{4}{3}} \varepsilon_{B,-2.5}^{\frac{7p-3}{12}} E_{iso,54}^{\frac{p}{8}-\frac{13}{12}} n_0^{\frac{5p}{12}-\frac{187}{72}} T_{obs,2}^{\frac{p}{8}-\frac{5}{4}} & \text{for } Y(\gamma_c) \gtrsim 1. \end{cases} \quad (B30)$$

These expressions show that \mathcal{F} decreases with increasing burst energy E_{iso} , circumburst density n , and observer time T_{obs} , with only a weak dependence on the electron spectral index p . For $p \simeq 2.4$, the expressions reduce to

$$\mathcal{F} \simeq \begin{cases} 17.7 \varepsilon_{e,-1}^{2.7} \varepsilon_{B,-2.5}^{0.02} E_{\text{iso},54}^{-0.28} n_0^{-0.95} T_{\text{obs},2}^{-1.15} & \text{for } Y(\gamma_c) < 1 \\ 2.2 \varepsilon_{e,-1}^{1.3} \varepsilon_{B,-2.5}^{-0.1} E_{\text{iso},54}^{-0.78} n_0^{-1.6} T_{\text{obs},2}^{-0.95} & \text{for } Y(\gamma_c) \gtrsim 1. \end{cases} \quad (\text{B31})$$

A large value of \mathcal{F} , corresponding to a more pronounced synchrotron cutoff, is therefore favored for low-energy explosions in low-density environments at early times. Increasing n raises the number of relativistic electrons and therefore the optical depth of synchrotron photons, enhancing SSC emission and reducing \mathcal{F} . Moreover, larger E_{iso} and n shift ν_c to lower frequencies, weakening KN suppression and increasing the Compton Y parameter, which further boosts SSC relative to synchrotron emission and suppresses \mathcal{F} .

At $T_{\text{obs}} \sim 10^3$ s, we typically have $\nu_{\text{max,PIC}} > \nu_m^{\text{IC}}$, and a similar procedure can be followed, yielding

$$\mathcal{F} \simeq \begin{cases} 2.3 \times 10^8 (1.2 \times 10^{-8})^{\frac{p}{2}} \left(\frac{p-2}{p-1}\right)^{2-p} \varepsilon_{e,-1}^{1-p} \varepsilon_{B,-2.5}^{-\frac{2}{3}} E_{\text{iso},54}^{-\frac{p}{8}-\frac{1}{2}} n_0^{\frac{p}{8}-\frac{4}{3}} T_{\text{obs},2}^{\frac{3p}{8}-\frac{1}{2}} & \text{for } Y(\gamma_c) < 1 \\ 1.7 \times 10^7 (1.2 \times 10^{-8})^{\frac{p}{2}} \left(\frac{p-2}{p-1}\right)^{4-2p} \varepsilon_{e,-1}^{2-2p} \varepsilon_{B,-2.5}^{\frac{p}{4}-\frac{17}{12}} E_{\text{iso},54}^{-\frac{p}{8}-1} n_0^{\frac{3p}{8}-\frac{31}{12}} T_{\text{obs},2}^{\frac{7p}{8}-\frac{3}{2}} & \text{for } Y(\gamma_c) \gtrsim 1. \end{cases} \quad (\text{B32})$$

For $p \simeq 2.4$, the expressions reduce to

$$\mathcal{F} \simeq \begin{cases} 0.12 \varepsilon_{e,-1}^{-1.4} \varepsilon_{B,-2.5}^{-0.7} E_{\text{iso},54}^{-0.8} n_0^{-1} T_{\text{obs},2}^{0.4} & \text{for } Y(\gamma_c) < 1 \\ 0.014 \varepsilon_{e,-1}^{-2.8} \varepsilon_{B,-2.5}^{-0.8} E_{\text{iso},54}^{-1.3} n_0^{-1.7} T_{\text{obs},2}^{0.6} & \text{for } Y(\gamma_c) \gtrsim 1. \end{cases} \quad (\text{B33})$$

In this regime, \mathcal{F} shows a modest increase with observer time. However, this behavior has limited practical relevance, as the time dependence is weak and the absolute values of \mathcal{F} are already substantially smaller than those at $T_{\text{obs}} \sim 100$ s. Moreover, late-time observations are more affected by source fading and background contamination, consistent with the shrinking detectability regions in Figure 2.

REFERENCES

Acciari, V. A., et al. 2019a, *Nature*, 575, 459, doi: [10.1038/s41586-019-1754-6](https://doi.org/10.1038/s41586-019-1754-6)

Acciari, V. A., et al. 2019b, *Nature*, 575, 455, doi: [10.1038/s41586-019-1750-x](https://doi.org/10.1038/s41586-019-1750-x)

Acciari, V. A., Ansoldi, S., Antonelli, L. A., et al. 2021, *ApJ*, 908, 90, doi: [10.3847/1538-4357/ab249](https://doi.org/10.3847/1538-4357/ab249)

Achterberg, A., Gallant, Y. A., Kirk, J. G., & Guthmann, A. W. 2001, *MNRAS*, 328, 393, doi: [10.1046/j.1365-8711.2001.04851.x](https://doi.org/10.1046/j.1365-8711.2001.04851.x)

Achterberg, A., & Wiersma, J. 2007, *A&A*, 475, 1, doi: [10.1051/0004-6361:20065365](https://doi.org/10.1051/0004-6361:20065365)

Ackermann, M., Ajello, M., Asano, K., et al. 2014, *Science*, 343, 42, doi: [10.1126/science.1242353](https://doi.org/10.1126/science.1242353)

Aguilar-Ruiz, E., Gill, R., Beniamini, P., & Granot, J. 2025, arXiv e-prints, arXiv:2511.23349, doi: [10.48550/arXiv.2511.23349](https://doi.org/10.48550/arXiv.2511.23349)

Ajello, M., Arimoto, M., Axelsson, M., et al. 2019, *ApJ*, 878, 52, doi: [10.3847/1538-4357/ab1d4e](https://doi.org/10.3847/1538-4357/ab1d4e)

Ajello, M., Arimoto, M., Axelsson, M., et al. 2020, *ApJ*, 890, 9, doi: [10.3847/1538-4357/ab5b05](https://doi.org/10.3847/1538-4357/ab5b05)

Aksulu, M. D., Wijers, R. A. M. J., van Eerten, H. J., & van der Horst, A. J. 2022, *MNRAS*, 511, 2848, doi: [10.1093/mnras/stac246](https://doi.org/10.1093/mnras/stac246)

Aleksić, J., Ansoldi, S., Antonelli, L. A., et al. 2016a, *Astroparticle Physics*, 72, 61, doi: [10.1016/j.astropartphys.2015.04.004](https://doi.org/10.1016/j.astropartphys.2015.04.004)

Aleksić, J., Ansoldi, S., Antonelli, L. A., et al. 2016b, *Astroparticle Physics*, 72, 76, doi: [10.1016/j.astropartphys.2015.02.005](https://doi.org/10.1016/j.astropartphys.2015.02.005)

Axelsson, M., Ajello, M., Arimoto, M., et al. 2025, *ApJS*, 277, 24, doi: [10.3847/1538-4365/ada272](https://doi.org/10.3847/1538-4365/ada272)

Barniol Duran, R., & Kumar, P. 2011, *MNRAS*, 412, 522, doi: [10.1111/j.1365-2966.2010.17927.x](https://doi.org/10.1111/j.1365-2966.2010.17927.x)

Bell, A. R. 1978, *MNRAS*, 182, 147, doi: [10.1093/mnras/182.2.147](https://doi.org/10.1093/mnras/182.2.147)

Beloborodov, A. M. 2002, *ApJ*, 565, 808, doi: [10.1086/324195](https://doi.org/10.1086/324195)

Beniamini, P., Nava, L., Duran, R. B., & Piran, T. 2015, *MNRAS*, 454, 1073, doi: [10.1093/mnras/stv2033](https://doi.org/10.1093/mnras/stv2033)

Beniamini, P., Nava, L., & Piran, T. 2016, *MNRAS*, 461, 51, doi: [10.1093/mnras/stw1331](https://doi.org/10.1093/mnras/stw1331)

Beniamini, P., & van der Horst, A. J. 2017, MNRAS, 472, 3161, doi: [10.1093/mnras/stx2203](https://doi.org/10.1093/mnras/stx2203)

Blandford, R. D., & McKee, C. F. 1976, Phys. Fluids, 19, 1130, doi: [10.1063/1.861619](https://doi.org/10.1063/1.861619)

Blandford, R. D., & Ostriker, J. P. 1978, ApJL, 221, L29, doi: [10.1086/182658](https://doi.org/10.1086/182658)

Burns, E., Svinkin, D., Fenimore, E., et al. 2023, ApJL, 946, L31, doi: [10.3847/2041-8213/acc39c](https://doi.org/10.3847/2041-8213/acc39c)

Caputo, R., Ajello, M., Kierans, C. A., et al. 2022, Journal of Astronomical Telescopes, Instruments, and Systems, 8, 044003, doi: [10.1117/1.JATIS.8.4.044003](https://doi.org/10.1117/1.JATIS.8.4.044003)

Chang, P., Spitkovsky, A., & Arons, J. 2008, International Journal of Modern Physics D, 17, 1769, doi: [10.1142/S021827180801339X](https://doi.org/10.1142/S021827180801339X)

Crowther, P. A. 2007, ARA&A, 45, 177, doi: [10.1146/annurev.astro.45.051806.110615](https://doi.org/10.1146/annurev.astro.45.051806.110615)

Curran, P. A., Evans, P. A., de Pasquale, M., Page, M. J., & van der Horst, A. J. 2010, ApJL, 716, L135, doi: [10.1088/2041-8205/716/2/L135](https://doi.org/10.1088/2041-8205/716/2/L135)

Davis, Z., et al. 2024, ApJ, 976, 182, doi: [10.3847/1538-4357/ad8bc2](https://doi.org/10.3847/1538-4357/ad8bc2)

de Jager, O. C., & Harding, A. K. 1992, ApJ, 396, 161, doi: [10.1086/171706](https://doi.org/10.1086/171706)

Derishev, E. V., & Piran, T. 2016, MNRAS, 460, 2036, doi: [10.1093/mnras/stw1175](https://doi.org/10.1093/mnras/stw1175)

Fermi, E. 1949, Physical Review, 75, 1169, doi: [10.1103/PhysRev.75.1169](https://doi.org/10.1103/PhysRev.75.1169)

Golant, R., Vanthieghem, A., Grošelj, D., & Sironi, L. 2025, ApJ, 986, 211, doi: [10.3847/1538-4357/add404](https://doi.org/10.3847/1538-4357/add404)

Grošelj, D., Sironi, L., & Beloborodov, A. M. 2022, ApJ, 933, 74, doi: [10.3847/1538-4357/ac713e](https://doi.org/10.3847/1538-4357/ac713e)

Grošelj, D., et al. 2024, ApJL, 963, L44, doi: [10.3847/2041-8213/ad2c8c](https://doi.org/10.3847/2041-8213/ad2c8c)

Harris, C. R., Millman, K. J., van der Walt, S. J., et al. 2020, Nature, 585, 357, doi: [10.1038/s41586-020-2649-2](https://doi.org/10.1038/s41586-020-2649-2)

He, X.-B., Tam, P.-H. T., Long, G.-B., et al. 2022, A&A, 657, A111, doi: [10.1051/0004-6361/202040039](https://doi.org/10.1051/0004-6361/202040039)

Hofmann, W., & Zanin, R. 2023, arXiv e-prints, arXiv:2305.12888, doi: [10.48550/arXiv.2305.12888](https://doi.org/10.48550/arXiv.2305.12888)

Huang, Z.-Q., Kirk, J. G., Giacinti, G., & Reville, B. 2022, ApJ, 925, 182, doi: [10.3847/1538-4357/ac3f38](https://doi.org/10.3847/1538-4357/ac3f38)

Hunter, J. D. 2007, Computing in Science and Engineering, 9, 90, doi: [10.1109/MCSE.2007.55](https://doi.org/10.1109/MCSE.2007.55)

Jacovich, T. E., Beniamini, P., & van der Horst, A. J. 2021, MNRAS, 504, 528, doi: [10.1093/mnras/stab911](https://doi.org/10.1093/mnras/stab911)

Keshet, U., Katz, B., Spitkovsky, A., & Waxman, E. 2009, ApJL, 693, L127, doi: [10.1088/0004-637X/693/2/L127](https://doi.org/10.1088/0004-637X/693/2/L127)

Kirk, J. G., & Reville, B. 2010, ApJL, 710, L16, doi: [10.1088/2041-8205/710/1/L16](https://doi.org/10.1088/2041-8205/710/1/L16)

Kumar, P., Hernández, R. A., Bošnjak, Ž., & Barniol Duran, R. 2012, MNRAS, 427, L40, doi: [10.1111/j.1745-3933.2012.01341.x](https://doi.org/10.1111/j.1745-3933.2012.01341.x)

Lemoine, M. 2013, MNRAS, 428, 845, doi: [10.1093/mnras/sts081](https://doi.org/10.1093/mnras/sts081)

Lemoine, M. 2015a, Journal of Plasma Physics, 81, 455810101, doi: [10.1017/S0022377814000920](https://doi.org/10.1017/S0022377814000920)

Lemoine, M. 2015b, MNRAS, 453, 3772, doi: [10.1093/mnras/stv1800](https://doi.org/10.1093/mnras/stv1800)

Longo, F., Bissaldi, E., Bregeon, J., et al. 2016a, GRB Coordinates Network, 19403, 1

Longo, F., Bissaldi, E., Vianello, G., et al. 2016b, GRB Coordinates Network, 19413, 1

Martins, S. F., Fonseca, R. A., Silva, L. O., & Mori, W. B. 2009, ApJL, 695, L189, doi: [10.1088/0004-637X/695/2/L189](https://doi.org/10.1088/0004-637X/695/2/L189)

Miceli, D., & Nava, L. 2022, Galaxies, 10, 66, doi: [10.3390/galaxies10030066](https://doi.org/10.3390/galaxies10030066)

Mimica, P., & Giannios, D. 2011, MNRAS, 418, 583, doi: [10.1111/j.1365-2966.2011.19507.x](https://doi.org/10.1111/j.1365-2966.2011.19507.x)

Nakar, E., Ando, S., & Sari, R. 2009, ApJ, 703, 675, doi: [10.1088/0004-637X/703/1/675](https://doi.org/10.1088/0004-637X/703/1/675)

Nava, L., Vianello, G., Omodei, N., et al. 2014, MNRAS, 443, 3578, doi: [10.1093/mnras/stu1451](https://doi.org/10.1093/mnras/stu1451)

Panaiteescu, A. 2017, ApJ, 837, 13, doi: [10.3847/1538-4357/837/1/13](https://doi.org/10.3847/1538-4357/837/1/13)

Pelloquin, C., & Daigne, F. 2024, A&A, 690, A281, doi: [10.1051/0004-6361/202347516](https://doi.org/10.1051/0004-6361/202347516)

Pennanen, T., Vurm, I., & Poutanen, J. 2014, A&A, 564, A77, doi: [10.1051/0004-6361/201322520](https://doi.org/10.1051/0004-6361/201322520)

Piran, T., & Nakar, E. 2010, ApJL, 718, L63, doi: [10.1088/2041-8205/718/2/L63](https://doi.org/10.1088/2041-8205/718/2/L63)

Plotnikov, I., Grassi, A., & Grech, M. 2018, MNRAS, 477, 5238, doi: [10.1093/mnras/sty979](https://doi.org/10.1093/mnras/sty979)

Plotnikov, I., Pelletier, G., & Lemoine, M. 2013, MNRAS, 430, 1280, doi: [10.1093/mnras/sts696](https://doi.org/10.1093/mnras/sts696)

Reville, B., & Bell, A. R. 2014, MNRAS, 439, 2050, doi: [10.1093/mnras/stu088](https://doi.org/10.1093/mnras/stu088)

Rhoads, J. E. 1997, ApJL, 487, L1, doi: [10.1086/310876](https://doi.org/10.1086/310876)

Rouco Escorial, A., Fong, W., Berger, E., et al. 2023, ApJ, 959, 13, doi: [10.3847/1538-4357/acf830](https://doi.org/10.3847/1538-4357/acf830)

Ruffini, R., Wang, Y., Enderli, M., et al. 2015, ApJ, 798, 10, doi: [10.1088/0004-637X/798/1/10](https://doi.org/10.1088/0004-637X/798/1/10)

Sagi, E., & Nakar, E. 2012, ApJ, 749, 80, doi: [10.1088/0004-637X/749/1/80](https://doi.org/10.1088/0004-637X/749/1/80)

Santana, R., Barniol Duran, R., & Kumar, P. 2014, ApJ, 785, 29, doi: [10.1088/0004-637X/785/1/29](https://doi.org/10.1088/0004-637X/785/1/29)

Sari, R., & Esin, A. A. 2001, ApJ, 548, 787, doi: [10.1086/319003](https://doi.org/10.1086/319003)

Sari, R., Narayan, R., & Piran, T. 1996, ApJ, 473, 204, doi: [10.1086/178136](https://doi.org/10.1086/178136)

Sari, R., & Piran, T. 1995, ApJL, 455, L143, doi: [10.1086/309835](https://doi.org/10.1086/309835)

Sari, R., Piran, T., & Halpern, J. P. 1999, ApJL, 519, L17, doi: [10.1086/312109](https://doi.org/10.1086/312109)

Sari, R., et al. 1998, ApJL, 497, L17, doi: [10.1086/311269](https://doi.org/10.1086/311269)

Sironi, L., & Spitkovsky, A. 2011, ApJ, 726, 75, doi: [10.1088/0004-637X/726/2/75](https://doi.org/10.1088/0004-637X/726/2/75)

Sironi, L., et al. 2013, ApJ, 771, 54, doi: [10.1088/0004-637X/771/1/54](https://doi.org/10.1088/0004-637X/771/1/54)

Sironi, L., et al. 2015, Space Sci. Rev., 191, 519, doi: [10.1007/s11214-015-0181-8](https://doi.org/10.1007/s11214-015-0181-8)

Spitkovsky, A. 2008a, ApJL, 682, L5, doi: [10.1086/590248](https://doi.org/10.1086/590248)

Spitkovsky, A. 2008b, ApJL, 673, L39, doi: [10.1086/527374](https://doi.org/10.1086/527374)

Tomsick, J., Boggs, S., Zoglauer, A., et al. 2024, in 38th International Cosmic Ray Conference, 745, doi: [10.22323/1.444.0745](https://doi.org/10.22323/1.444.0745)

Troja, E., Castro-Tirado, A. J., Becerra González, J., et al. 2019, MNRAS, 489, 2104, doi: [10.1093/mnras/stz2255](https://doi.org/10.1093/mnras/stz2255)

Virtanen, P., Gommers, R., Oliphant, T. E., et al. 2020, Nature Medicine, 17, 261, doi: [10.1038/s41592-019-0686-2](https://doi.org/10.1038/s41592-019-0686-2)

Wang, H., Dastidar, R. G., Giannios, D., & Duffell, P. C. 2024, ApJS, 273, 17, doi: [10.3847/1538-4365/ad4d9d](https://doi.org/10.3847/1538-4365/ad4d9d)

Wang, X.-G., Zhang, B., Liang, E.-W., et al. 2018, ApJ, 859, 160, doi: [10.3847/1538-4357/aabc13](https://doi.org/10.3847/1538-4357/aabc13)

Yamasaki, S., & Piran, T. 2022, MNRAS, 512, 2142, doi: [10.1093/mnras/stac483](https://doi.org/10.1093/mnras/stac483)